Macromolecules 2004, 37, 2171−2181

Atomic Force Microscopy Observations on the Structure Development during Uniaxial Stretching of PP from Partially Molten State: Effect of Isotacticity

Yutaka Koike and Miko Cakmak*

Institute of Polymer Engineering, The University of Akron, Akron, Ohio 44325-0301

Received May 2, 2003

ABSTRACT: Our main focus is to investigate the role of isotacticity on the development of morphology in PP films uniaxially deformed from the partially molten state. Polypropylene films with low isotactic index 43 exhibit crosshatched lamella. At the early stages of deformation, this morphology is first broken into small pieces and then microfibrils start to appear. As the deformation proceeds, this morphology transforms from primarily shish kebab morphology to a more fibrillar superstructure with sparse population of laterally grown lamellae along their lengths. The microfibrils 15−20 nm in diameter are observed in isotactic index 43 and isotactic index 64. Thus, a macrofibril is composed of ca. 100 microfibrils along the width of macrofibrils that are more ribbonlike with the width of the ribbons coinciding with the *b*-axis. A nodular superstructure that contains one or more alternating lamella−amorphous pairs was found to be promoted at lower processing temperatures, lower stretching speed, and higher isotacticities. In low-tacticity PP, upon deformation the formation of a three-dimensional crystalline/entanglement network was found to exert hydrostatic pressure in the amorphous regions that lead to their highly localized blooming out of the surface. Room temperature aging was found to coalesce these amorphous regions—a process that resembles the late stages of phase separation in partially miscible systems.

1. Introduction

The study of morphology as influenced by material thermal/deformation history historically has been carried out with TEM. Although this technique requires special preparation conditions that allows for artifacts, it helped contribute to elucidatation of the deformation mechanisms in semicrystalline polymers. Some of these studies investigated the details of structural changes from spherulitic to fibrillar structure as a result of deformation. In the deformation model they considered twinning, tilt and slip, and twisting.[1−3] In addition, the local deformation mechanism depends on the orientation of the local lamellae axes with respect to the stretching direction.[4,5] Shimamura has clearly shown that the deformation mechanism depends on the drawing temperature.[6] He observed the polar region in the polyethylene spherulite deforms first at 0 °C, while the equatorial region deforms first at 100 °C.

AFM has become a morphological tool to investigate the surface topology of materials at a wide range of length scales. Primary research activities in this area have been concentrated on the isotropic as-cast polymers,[7−9] including low-isotacticity polypropylene.[10] Solid-state[11,12] and melt deformation effects have also been investigated.[13−16] The effect of deformation at elevated temperature was studied in ref 17, with the effect of deformation to engineering strain 6 at 140 °C, 2 mm/min on stretched isotactic polypropylene film with isotactic index 94. This study revealed the presence of fibrillar structure with some grains that are proposed to have epitaxially grown on the shish crystals (microfibrils).

In the film stretching of polypropylene it is typically cast into an unoriented highly crystalline state. This cast film is then heated to temperatures where the film partially melts, and deformation takes place at these “mushy” temperature regions where the melt and crystal forms of the same material coexist. These temperatures are very important from not only an industrial but also an academic point of view as industrial deformation of these materials is routinely performed in these partially molten (mushy) temperatures where these conditions are considered optimum conditions. There, however, is very little open literature on the dynamical behavior and morphology development in these materials as they are stretched and held in the film stretching machines. For example, as far as we know, most of the research has been concentrated on melt spinning, blown film, or injection molding. In these processes the complex deformation histories are imposed under nonisothermal conditions. It is therefore hard to elucidate the temperature effect on the deformation. Since the structural hierarchy very much depends on the thermal deformation history imposed on the materials, it is best to simplify this by restricting the deformation to constant temperature while investigating the deformation effect.

Evolution of structural hierarchy that includes crystallinity, crystallite size, and orientation depends not only on the thermal deformation history but also the level of tacticity present in polypropylene.[18−21] In addition, the increase of tacticity was found to enhance its toughness[22,23] and thermal properties.[18] However, the increase of tacticity causes the deformation of PP to be nonuniform by increasing the conditions for formation of necks during uni- and biaxial deformation in partially molten states typically practiced in the industry. This necking problem can be altered with reduction of crystallite size and chemical modification such as copolymerization with ethylene or changing tacticity. Recent developments in catalysis[24−26] allowed

---

* Corresponding author: Tel +1-330-972-6928; Fax +1-330-258-2339; e-mail cakmak@uakron.edu.

10.1021/ma030250a CCC: $27.50

Table 1. Basic Properties of Materials[a]

material maker	grade	MFR, g/10 min 230 °C	tacticity (%) mmmm	tacticity (%) rrrr
Idemitsu PetroChemical	E2700	2.5	64	9
Huntsman	WL111	1.5	43	12

[a] Xylene-insoluble fraction (wt %).

Table 2. Thermal Properties of Materials

isotactic index (%)	DSC (ramp = 10 °C/min) mp, °C start	onset	peak	end	T_c (°C) peak	crystallinity (%)
64	111	142	157	167	105	24
43	85	127	153	164	88	14

the commercialization of low-tacticity polypropylene. This, in turn, is allowing the production of PP's with a wide range of properties from hard plastic to as soft as plastisized poly(vinyl chloride) with minimal decrease in thermal properties. Waymouth et al. extensively studied structure and thermal and mechanical properties of PP with tacticities ranging from 21 to 76 in mmmm (isotactic pentad).[26−33] Melt-pressed films of these materials showed crosshatching lamellae, hedrites, and spherulitic structure using AFM.

To our knowledge, the effect of isotacticity on deformation behavior and morphological development at partially and wholly molten state has not been investigated.

To unravel the sequence of structural mechanisms that take place during uniaxial deformation at the partially molten state, we have extensively analyzed the films stretched under the constant temperature using AFM coupled with DSC and WAXS techniques. It represents a continuation of our earlier work on deformation structure property relationships in high-[34,35] and low-isotacticity PP.[36]

2. Experimental Procedures

2.1. Materials. Table 1 shows the details of the three types of PP used in this research, including the MFR and isotacticity quantified by the xylene-insoluble method based on ISO 9113: 1986 for high-isotacticity PP or isotactic pentad (mmmm) and syndiotactic pentad (rrrr) content measured by NMR[37,38] for low-isotacticity PP. In this paper, we distinguish the materials by the presence of percentage of the xylene-insoluble fraction or isotactic pentad content called the isotactic index[39] (64 and 43 in decreasing isotacticities). A TA Instruments DSC 2920 was used to determine the melting point (mp) at a heating rate of 10 °C/min. Crystallinity (X_c) is obtained using eq 1. The thermal property is shown at the Table 2.

(a) Isotacticity Index 64 150°C 300mm/min

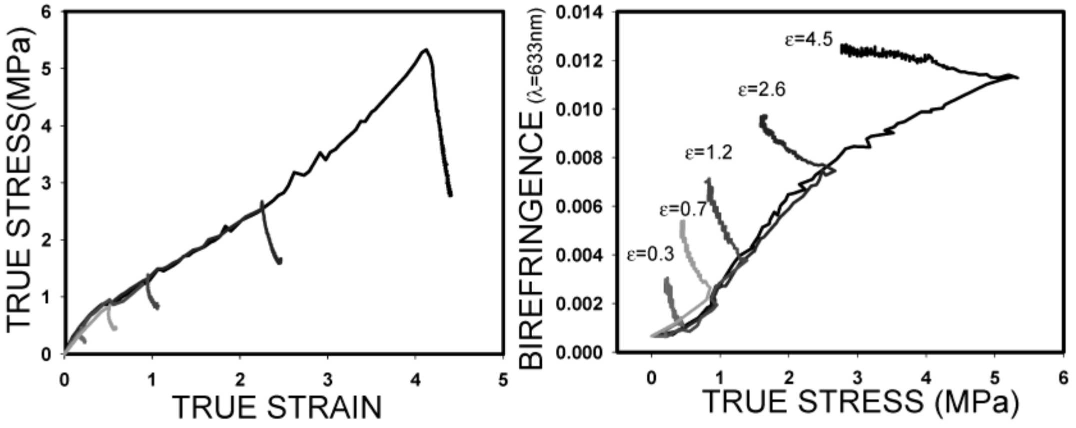

(b) Isotacticity Index 43 140°C 300mm/min

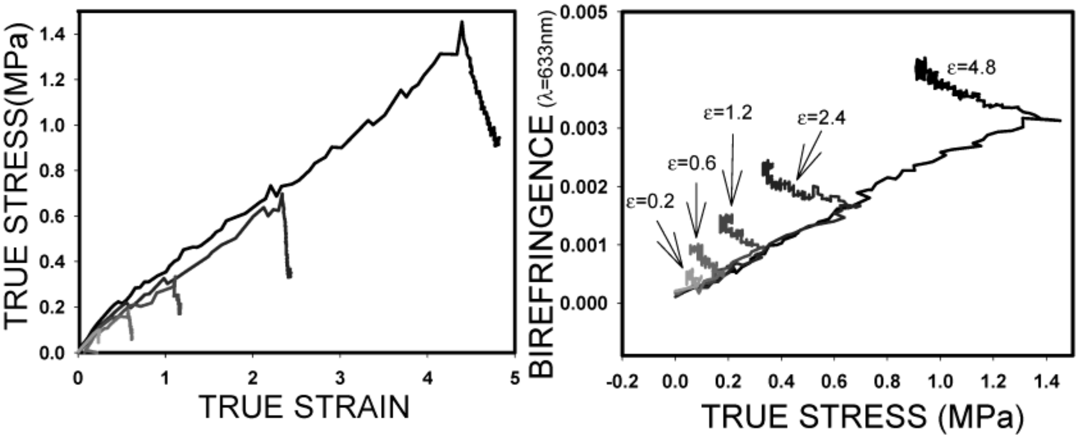

Figure 1. Examples of mechanical data.

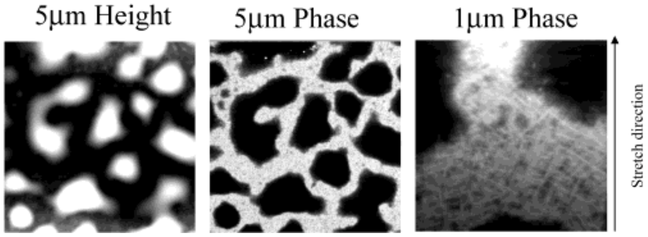

Figure 2. AFM images of film surface of as cast of isotactic index 43 (length means full scale).

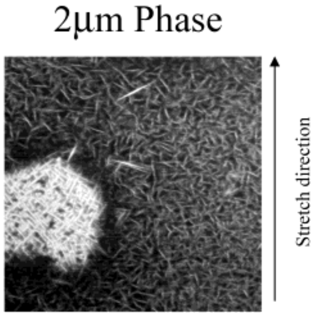

Figure 3. AFM images of film surface of holded 140 °C for 10 min of isotactic index 43 (length means full scale).

$$X_c\,(\%) = \text{enthalpy of fusion}/\Delta H° \tag{1}$$

$$\Delta H° = 209\ \text{J/g}^{40}$$

2.2. Sample Preparation. Isotactic index 64 sheets of about 0.3 mm thickness were obtained by extrusion-casting using a 1 in. Prodex extruder (230 °C) equipped with an 8 in. sheet casting die onto a casting roll maintained at 40 °C. Isotactic index 43 films were obtained by compression molding at 230 °C and quenched into a water bath maintained at room temperature. Birefringence measurements of these films revealed them to be nearly isotropic. The films were cut into dumbbell shape with narrowest width of 30 mm at 30 mm gauge when target final strain is over 2.5 and narrowest width of 16 mm at 30 mm gauge when target final strain is below 2.5. The stretching direction was chosen as the original extrusion direction of the cast films.

The mounted samples were inserted into the sample chamber (see ref 34 for details) and equilibrated at the chosen temperature for 10 min. After this time, the samples were stretched with 2, 20, and 300 mm/min stretching rate until engineering strain level has reached 5.5. After the completion of stretching the samples were held in the clamps for 10, 12, and 40 min after stretching with 300, 20, and 2 mm/min stretching rate, respectively. As described earlier in the paper for isotactic index 64 samples 125, 140, 150 °C for isotactic index 64 and for isotactic index 43 100, 125, 140 °C stretching temperatures were used. Note that the optimum processing temperatures for isotactic index 64 and isotactic index 43 were selected as 150 and 140 °C per the following criterion typically used in industry (eq 2).

$$T_{\text{stretch}} = T_{\text{onset temperature of melting}} + (T_{\text{end of melting}} - T_{\text{onset of melting}})/3 \tag{2}$$

After stretching, the samples were cooled by an air blower to room temperature and then removed from the clamps and stored in a refrigerator at −20 °C except during measurements of offline experiments such as DSC, WAXD, and AFM. We did not observe significant shrinkage in these series of experiments. Typical true stress−true strain and birefringence−true stress data for isotactic index 64 and isotactic index 43 are shown in Figure 1a,b. At higher isotacticity the birefringence vs true stress data indicate the birefringence begins to increase substantially beyond a yielding, and in the second stage where substantial plastic deformation takes place the relationship is nearly linear. Beyond about 2−3 MPa it becomes nonlinear. For isotactic index 43 this relationship was found to be linear throughout the whole stress levels, signifying that the stress−optical rule is obeyed at low isotacticities. During relaxation associated with holding all the data indicate the increase of birefringence while stresses decrease.

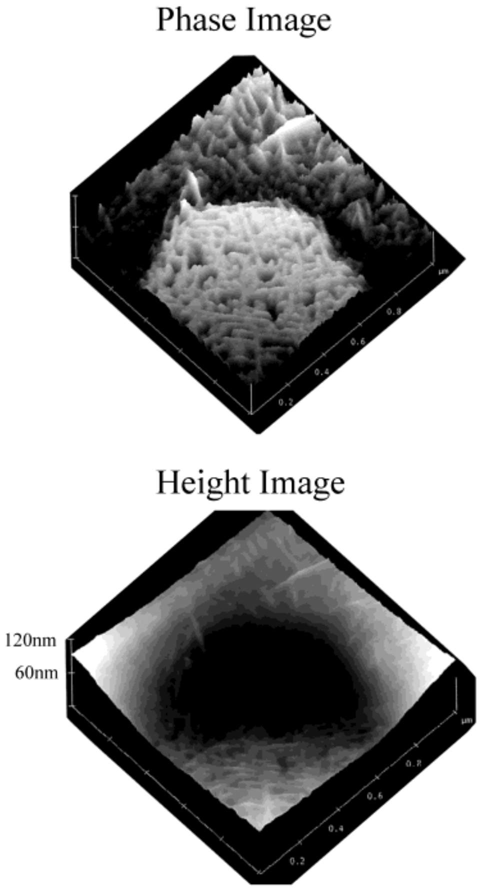

Figure 4. AFM 3D image of film surface at the same place as Figure 3.

2.3. Measurements of AFM. A Digital Instruments Nanoscope IIIa multimode scanning probe microscope was used in Tapping Mode. Nanodevices FESP, that is a noncoated Si probe and its frequency 60−80 kHz, is used as a probe. Samples were observed as stretched state without added surface treatments. The experiments were performed at room temperature. The samples are measured at room temperature. The images are obtained as height images and phase images. Bright regions in the height image represent elevated regions. In the phase image brighter regions represent harder regions. In all cases, the stretching direction is vertical in all images as indicated by an arrow in the figures.

2.4. X-ray Measurements. A Bruker AXS Generator equipped with a copper target tube and two-dimensional detector was used to obtain the unique one quadrant of the uniaxially oriented samples. The generator was operated at 40 kV and 40 mA, and the beam was monochromatized at Cu Kα . The samples were irradiated for 3 min.

3. Results and Discussion

3.1. Lower Isotacticity Films (Isotactic Index 43).

Height and phase images of low-tacticity cast films of isotactic index 43 are shown in Figure 2 at different length scales. We observe two distinct morphological features: bright regions in height images correspond to dark regions in the phase image. These regions correspond to amorphous regions as they are softer and appear darker in phase images. The height image suggests that they are bloomed out to the surface. The

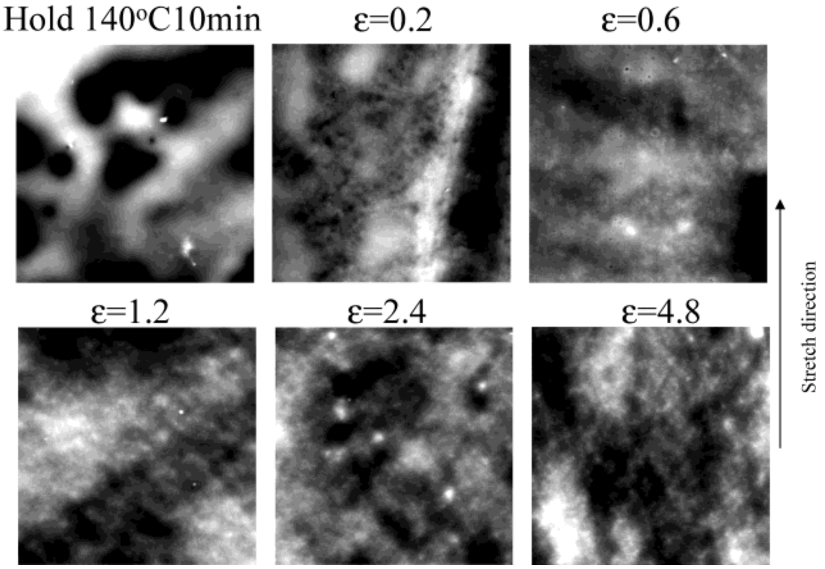

Figure 5. AFM images of film surface of stretched at 140 °C of isotactic index 43 (full scale 20 μm, height image).

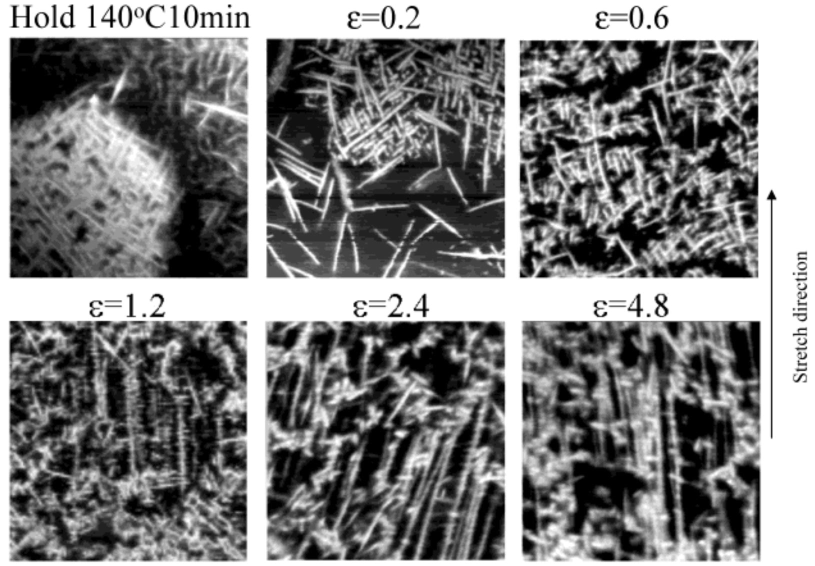

Figure 6. AFM images of film surface of stretched at 140 °C of isotactic index 43 (full scale 1 μm, phase image).

bright regions in the phase image correspond to the crystalline regions that show long-range connected network appearance. In the 1 μm full scale phase image of the isotactic index 43 sample shown in Figure 2, the dominant morphology in these crystalline regions is crosshatched lamellae.[10,41,42] In isotactic index 43 we do not see larger spherulitic formations as is typical in the high-tacticity PP's.[7,13,15,16,35]

To investigate the effect of holding time at the processing temperature prior to stretching, we subjected the cast films of isotactic index 43 to annealing at 140 °C for 10 min. The data indicate that the crystallization occurs in previously amorphous regions and crosshatched morphology becomes even more widespread throughout the surface. In these images crystallite lengths are around 0.4 μm. For better clarity, Figure 4

shows 3-D images of a high-resolution image shown in Figure 3. The thickness of the amorphous-rich layer is roughly 100 nm. The angle between the tangential lamella and radial lamella is in the 79°−85° range. This is close to the reported value 80°40′ [41] for the crosshatched lamellar morphology.

Figures 5 and 6 show AFM images of isotactic index 43 films stretched to a series of deformation levels at 140 °C with 300 mm/min stretching rate. The structure in the crystalline regions still exhibit crosshatched morphology even at strain levels of 0.6, indicating that the initial crosshatched structure is broken into small mostly unconnected pieces but crystallinity is so low—around 10%—that the major portion of the deformation is primarily taking place in the amorphous regions while crystalline regions acting as solid fillers. This observation is in accord with the fact that these films obey the stress optical rule (Figure 2). We also observe that amorphous-rich regions on the surface disperse more uniformly beyond the strain level of 1.2. At strains higher than the latter value, the microfibrillar morphology begins to appear among the field of large number of crosshatched lamellae. Although the fraction of broken crosshatched lamella decreases with further stretching, they still persist even at very high strain of 4.8 (Figure 6). The microfibrils of 18 nm diameter observed at strain level of 3 decrease to about 16 nm at a strain level of 4.8 obtained from image analysis of Figure 6. We also observe some of the microfibrils show kebab-like lateral overgrowths at strain range of 1.2 and

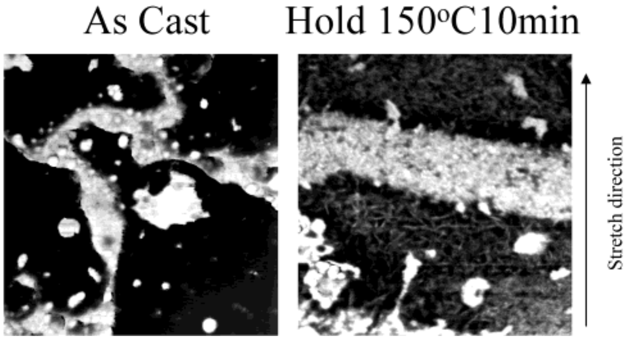

Figure 7. AFM images of film surface of isotactic index 64 (full scale 2 μm, phase image).

2.4, but they are not visible at high strains around 4.8. At this point, their origin is not clear. They could form after the deformation as lateral overgrowths on the microfibrils from molten and/or amorphous regions or remnants of the broken up crosshatched lamellae. The shish-kebab structure appears around 100−200% strain, and at higher strains 400% shish remains while kebabs disappear.[43] This result matches our results. The kebab periodicity is ca. 25 nm along the microfibril, and its length is ca. 60 nm. On the other hand, the length of the remnants of crystallites is 25−250 nm shown at 4.8 strain levels (Figure 6). Here kebabs are attached to shish at relatively regular interval, while the remnants are either distributed randomly along the shishes or they are entirely independent of these shishes.

3.2. Higher Isotacticity Films (Isotactic Index 64). Figure 7 shows the AFM phase images of as-cast and annealed isotactic index 64 sample. Ball-like structures of 80 nm appear between crystallites or in the amorphous regions. Annealing substantially enhances the definition of surface in the crystallite region. We also

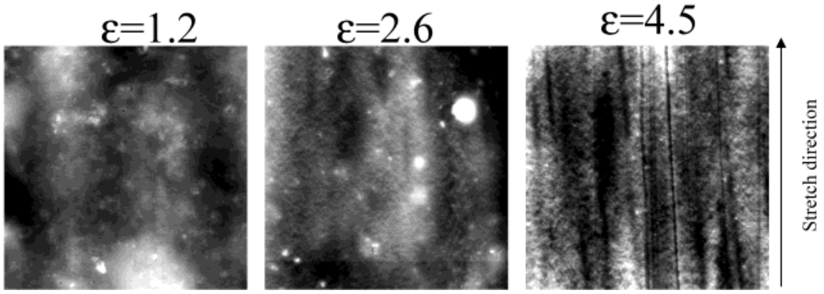

Figure 8. AFM images of film surface of isotactic index 64 (full scale 20 μm, height image).

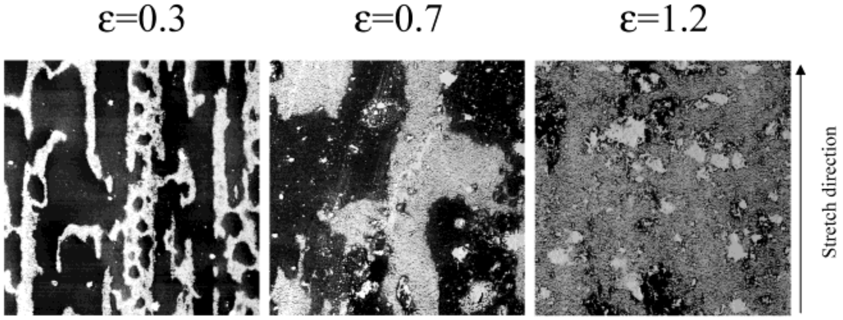

Figure 9. AFM images of film surface of isotactic index 64 (full scale 20 μm, phase image).

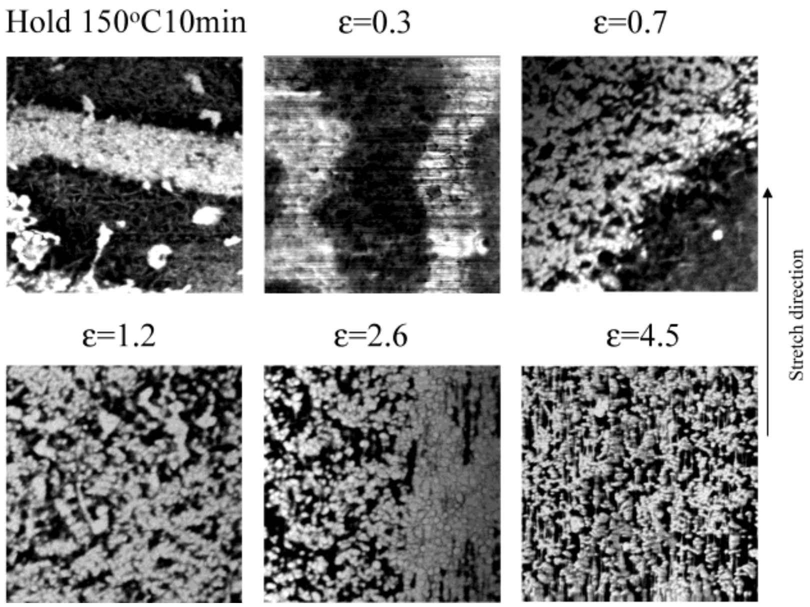

Figure 10. AFM images of film surface of stretched at 150 °C of isotactic index 64 (full scale 2 μm, phase image).

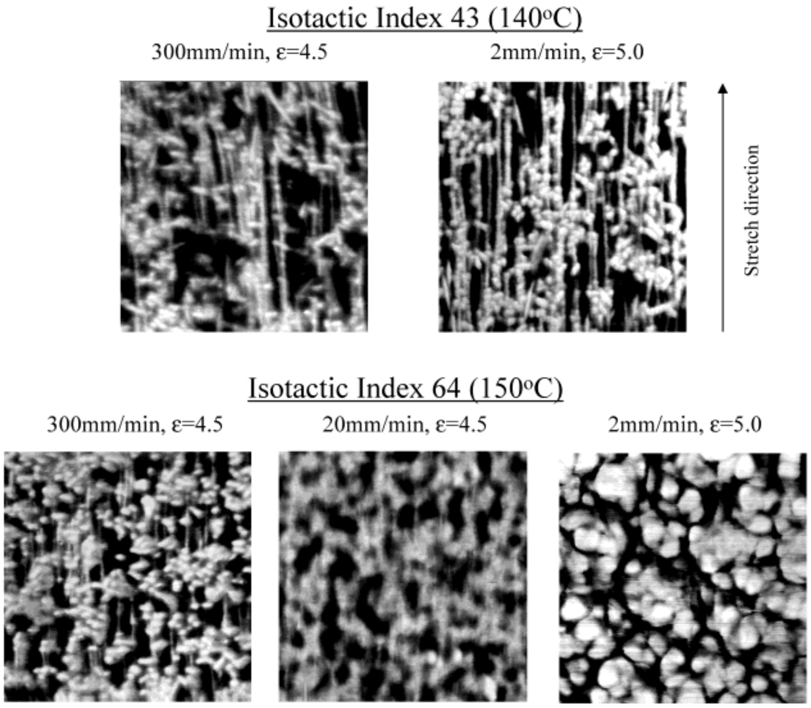

Figure 11. AFM images of film surface on stretch rate effect (full scale 1 μm, phase image).

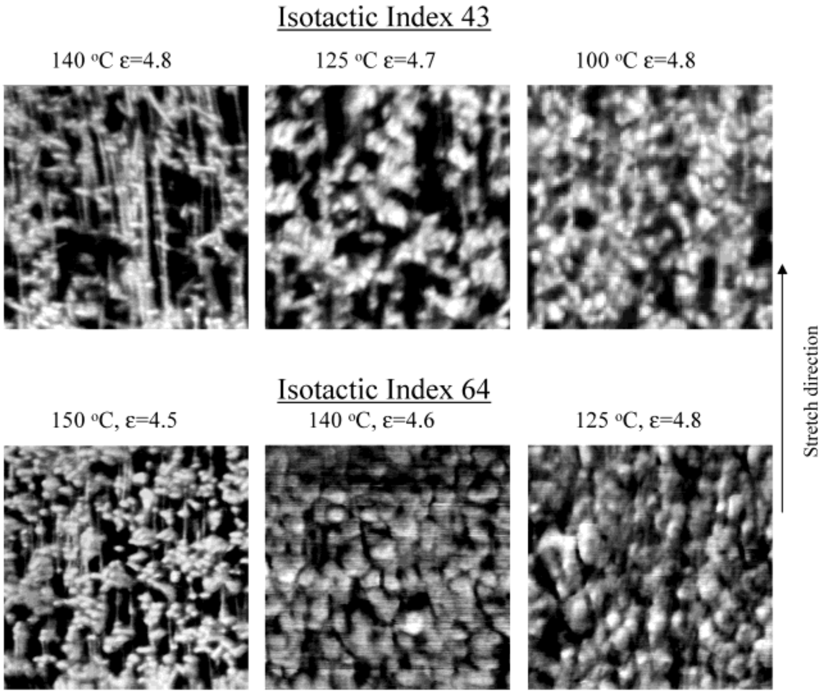

Figure 12. AFM images of film surface on stretch temperature effect at 300 mm/min (full scale 1 μm, phase image).

observe the appearance of crystallites in originally amorphous regions, but crosshatched morphology observed in lower tacticity PP is essentially absent.

Figures 8−10 show AFM images of films of samples stretched at 150 °C at 300 mm/min rate. The primarily amorphous (dark) regions gradually filled with crystallites (strain of 1.2 Figure 9), and this behavior is very similar to isotactic index 43. The microfibrils start to appear at the strain levels of 2.6. This microfibrillar appearance in the low-tacticity 43 sample was observed at lower strains. Ball-like crystalline regions give way to microfibrillar morphology at strain of 4.5 while some of their remnants still remain observable in Figure 10.

3.3. Effect of Stretching Conditions. Figure 11 shows the effect of stretching rate for samples stretched to large deformation levels. They all exhibit shish-kebab morphology. The increase of rate causes a decrease of size of lamellae. The size of the ball-like entities increases with the decrease of stretching rate. It should be noted that increased exposure to processing temperatures with lower rates of stretching could have played a role in the size enhancement of these ball-like entities.

Lowering the stretching temperature (Figure 12) has the same effect as decreasing the stretching speed shown in Figure 11. There is one exception, however, that the shapes of the ball-like entities are ellipsoidal

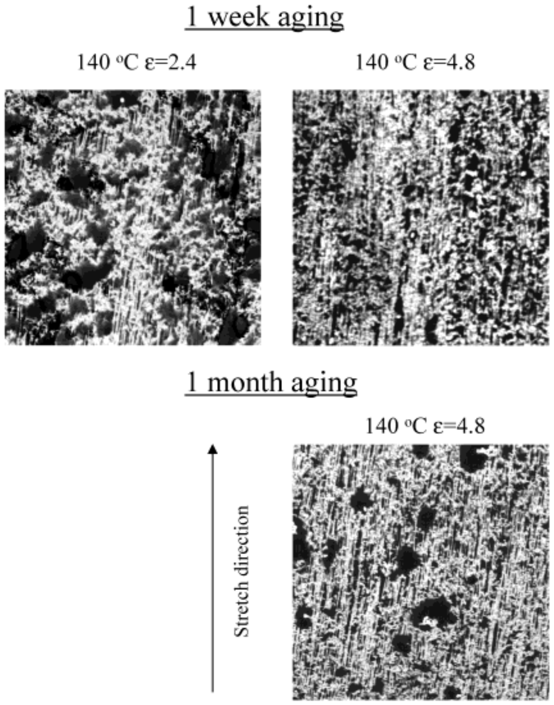

Figure 13. AFM images of film surface on aging effect for 1 week at room temperature; strain effect in isotactic index 43 (full scale 5 μm, phase image).

with their long axes oriented in the stretching direction (isotactic index 64, 125 °C, in Figure 12). This indicates that deformation becomes more homogeneous at lower temperatures at these length scales, perhaps reflecting the increased efficiency of transmission of forces to microscale structures. Another possibility is as follows: Upon cooling from melt, the higher isotacticity isotactic index 64 films exhibit higher crystallization peak temperature (105 °C) as compared to lower isotacticity isotactic index 43 films (88 °C). Obviously this is a direct consequence of increased crystallizability with increased isotacticities present in the samples. The fact that we observe larger nodules in higher isotacticity isotactic index 64 samples as compared to isotactic index 43 samples at comparable temperatures suggests that these nodules formed of mostly epitaxially grown crystallites on microfibrils.

3.4. Aging Effects. Since the T_g of isotactic index 43 is below 0 °C, room temperature, aging is expected to play a role in the long-term morphological development. These studies are shown in Figures 13−15. As we pointed out earlier, the dark regions represent softer amorphous regions. They have a tendency to bloom out of average surface plane. The films processed to lower strains (Figure 13) and the lower temperatures (Figure 14) exhibit larger amorphous regions that appear dark in these images. Figures 14 and 15 show the AFM images of the samples aged at room temperature for 1 week and 1 month. As these films age, the size of these amorphous regions increases. As the stretching temperature decreases, we observe that the amorphous regions coalesce into larger regions upon aging. This suggests that the processes governing this rearrangement are perhaps controlled partly by phase separation as the less crystallizable polymer chains or segments of chains containing lower isotacticity levels are phase separated into their own regions during this aging process.[44] Crystalline regions appearing as brighter regions continue to densify. This is particularly true in 140 °C stretched and aged samples.

Although it represents mostly bulk information, additional evidence comes from DSC analysis. Figure 16 show the DSC curves for isotactic index 43 films, indicating they change substantially by annealing or varying stretching temperature. These results also reveal that little or no change in crystallinity is observed even upon annealing. The melting peak becomes broader at the lower temperature stretching, signifying destruction of crystallites into smaller and/or more imperfect states. This size reduction seems to help the amorphous chain to bloom out to the surface; that is, the smaller size of crystallites with lower stretch temperature creates a more “open” structure. In addition, this latter process leads to recrystallization of some of the amorphous chains, compensating for the destruction effects on the original crystals. This scenario would explain why the total crystallinity remains roughly constant.

Figure 17 shows the DSC curves in isotactic index 64. Crystallinity increases by annealing and decreases with stretching in isotactic index 64. The melting peak shape changes are similar to those of isotactic index 43, but they are less pronounced.

Table 3 and Figure 18 show the crystallite size obtained by the Scherrer equation (eq 3) obtained from WAXD data.

$$\text{crystallite size; } L\ (\text{Å}) = K\lambda/(\beta_{1/2}\cos(\theta)) \tag{3}$$

Here, $K = 1$, λ is the wavelength of Kα = 1.542 Å, $\beta_{1/2}$ is the half-width, and θ is the peak position. We observe a significant increase in crystallite size with annealing after simulating holding stage in the film prior to stretching, confirming the surface observations are valid in the bulk of the samples as well (Table 3). Though the crystallite sizes obtained by WAXD represent average shown in Figure 18, they match well with the ones measured AFM pictures discussed before. We can see that crystallite size decreases with decreasing stretch temperature (Figure 18b,d). Because the ones stretched

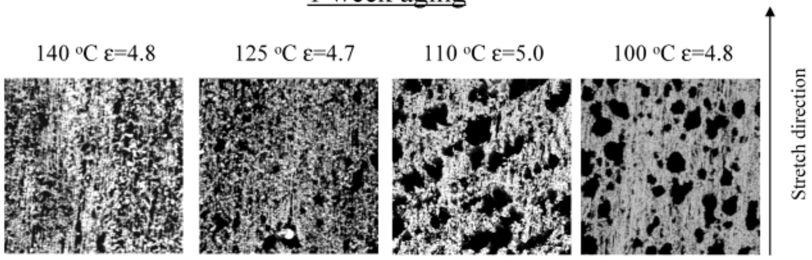

Figure 14. AFM images of film surface on aging effect for 1 week at room temperature; stretch temperature effect in isotactic index 43 (full scale 5 μm, phase image).

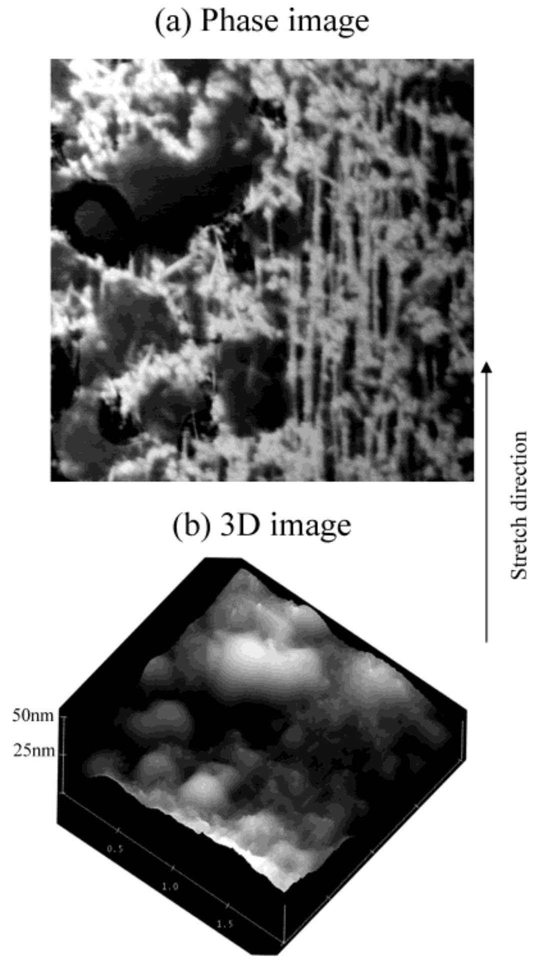
(a) Phase image

(b) 3D image

Figure 15. AFM 3D images of film surface on aging effect for 1 week at room temperature (isotactic index 43, 140 °C, 300 mm/min, true strain = 2.4; full scale 2 μm).

in the lower temperature have a significant amount of nodules, we are unable to verify the fibril size changes with AFM. On the other hand, it does not change with the stretch rate (Figure 18a,c).

3.5. Structural Model. The decrease of isotacticity increases the fraction of amorphous regions in these films, and at isotactic index 43 the crystalline regions are essentially unconnected; the resulting dynamic behavior shown at Figure 1 indicates that major fraction of deformation is taking place in the amorphous regions. The crystallites, although mainly locally connecting structures, are separated in amorphous regions at early stages of deformation. The structural conversions are taking place mostly in the amorphous regions typically undergoing strain-induced crystallization by forming the “shish structures” followed by the kebab overgrowths (Figure 6). We also observe some unusual behavior on the rate effect and temperature effects on the nodule formations. Lowering stretching rate and stretching temperature cause the nodules sizes to increase (Figures 11 and 12). Aging has a remarkable effect of phase segregating the amorphous regions, while crystalline regions densify (Figures 13−15).

Figure 19 shows a schematic of the relation between property and change of structure at the optimum processing temperature shown earlier (eq 2) in isotactic index 43 and isotactic index 64. We divided the behavior into three stages in the previous paper,[34] but isotactic index 43 in this condition show no stage I as shown in Figure 1. We attribute this to the presence of very low levels of crystallinity in these samples, resulting in rubberlike deformation of mostly amorphous chains and absence of long-range connectivity between the crystallites.

At the initial part in the stage II, the ball-like crystallites spread out in isotactic index 64 (Figure 10), or crosshatched lamella are broken into small pieces in isotactic index 43 (Figure 6). The microfibrils start to appear at stage II which corresponds to strain 1.2 in isotactic index 43 and 2.6 in isotactic index 64. We can see that shish-kebab-like structure in isotactic index 43 or the agglomerated crystallite in isotactic index 64 at this stage. At this stage the fibrillar structure develops well, and kebabs are not noticeable in stage III. But there remains substantial lamella on the microfibrils randomly distributed along their length. Isotactic index 64 shows the macrofibrils (Figure 8), while isotactic index 43 does hardly in this stage (Figure 5).

Figure 20 shows the further detailed structural model in microscale at these conditions. There are substantial amounts of nodules, but they do not appear to contribute to deformation mechanisms considered here. That is why we do not consider the existence of nodules here. AFM results showed that the structures are composed of macrofibrils of 3−5 μm in width (Figure 8) that are composed of microfibrils of 15−20 nm (Figure 10) in isotactic index 64. The latter values match well with the crystallite size obtained by WAXD (Figure 18c), even though it represents bulk property. The periodicity of microfibrils is roughly 300−400 nm in both isotactic index 43 (Figure 6) and isotactic index 64 (Figure 10). Thus, a typical macrofibril consists of ca. 100 microfibrils along their transverse direction in isotactic index 64. The *b*-axes are oriented in the transverse direction in the microfibrils. Since the *b*-axis is 2 nm long, a crystallite has 5−10 chains along *b*-axis. If we take the periodicities observed along the shish-kebab structures as representations of long periods, they are in the range of ca. 20−30 nm at strain 1.2−2.4 in isotactic index 43 (Figure 6).

Figure 21 shows the schematic of the structure in each stretch condition to explain the blooming of amorphous regions on the surface. The molecules connected with crystallites represent the gray line, and the unconnected ones represent the black line in Figure 21. At low strains, there are fewer numbers of the chains connected with crystallites. In the companion paper, we observed that the orientation function of amorphous chains is almost zero even at higher strain levels in isotactic index 43.[36] So most of the unconnected amorphous chains are in a random coil state. Once the strain becomes larger, the number of tie molecules will increase and the network of microfibrils consisting of crystallites will densify, thereby suppressing the mobility of unconnected crystallites. On the other hand, the size of each crystallite decreases with decreasing temperature (Figure 18b,d), resulting in generation of larger fraction of unconnected crystallite to go through the crystalline regions. We can also consider the barrier effect of crystallite to passage of free amorphous chain also decreases when crystallites become smaller. Blooming may have formed as follows: During crystallization from melt under deformation, a network of crystallites that are enhanced by chain entanglements form and start exerting hydrostatic pressure on the noncrystallizable chains of low tacticity and/or still molten regions..

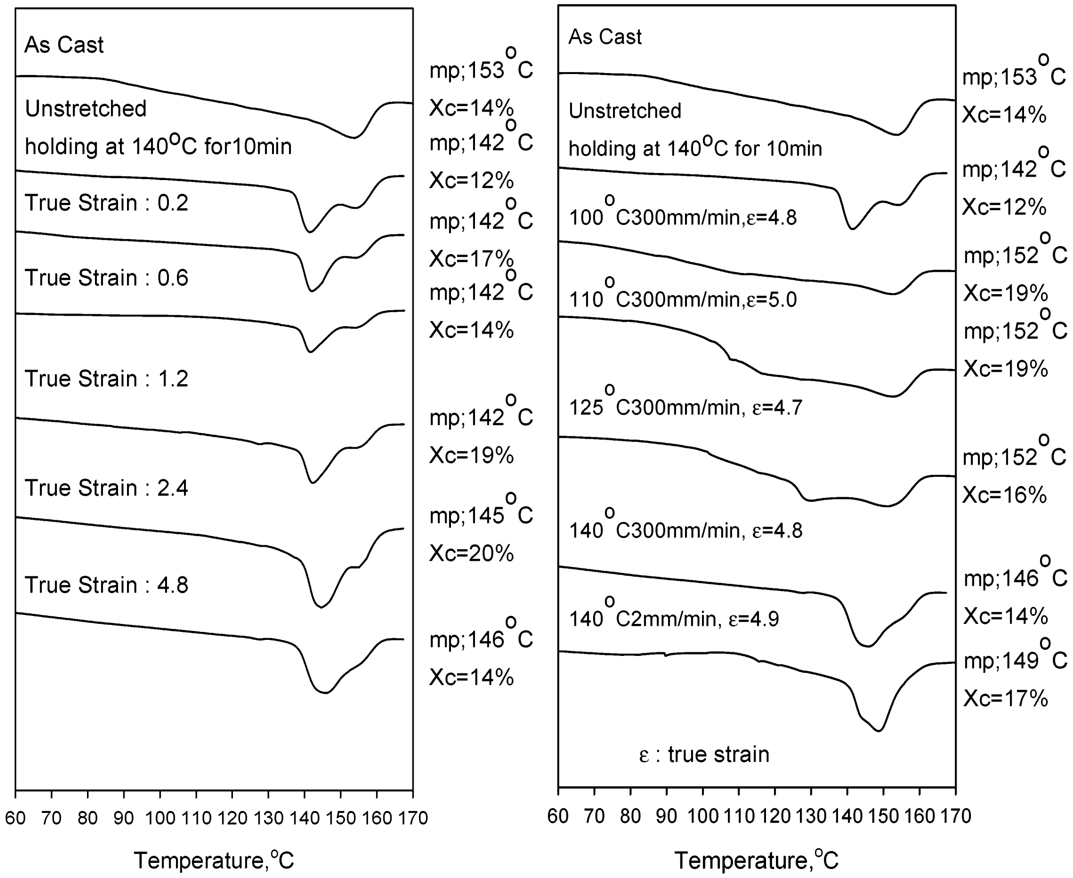

Figure 16. DSC curves dependent on the stretch conditions of isotactic index 43.

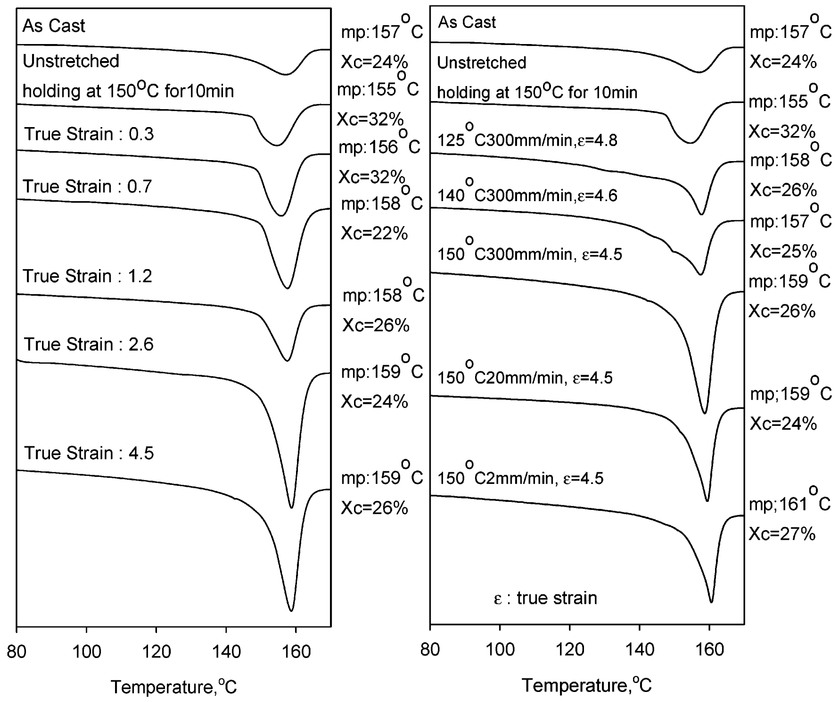

Figure 17. DSC curves dependent on the stretch conditions of isotactic index 64.

This leads to blooming at the surface. Obviously densification due to crystallization has a further amplifying effect on this mechanism During aging at room temperature, structural reorganization continues to occur, and thus amorphous-rich regions that contains mostly lower tacticity chains or segments of chains coalesce to enlarge these regions.

4. Conclusions

Low-isotacticity polypropylene film (isotactic index 43) exhibits crosshatched lamella. At the early stages of deformation, the latter morphology is first broken into small pieces and then microfibrils start to appear. At intermediate deformation levels, shish-kebab-like struc-

Table 3. Crystallite Size

isotactic index	lattice plane indices	crystallite size in the normal to the (*hkl*) crystal plane, Å: as cast	crystallite size in the normal to the (*hkl*) crystal plane, Å: anneal 10 min[a]
43	(110)	28	164
	(040)	66	157
	(130)	44	154
64	(110)	30	162
	(040)	51	186
	(130)	36	171

[a] Isotactic index 43: 140 °C; isotactic index 64: 150 °C.

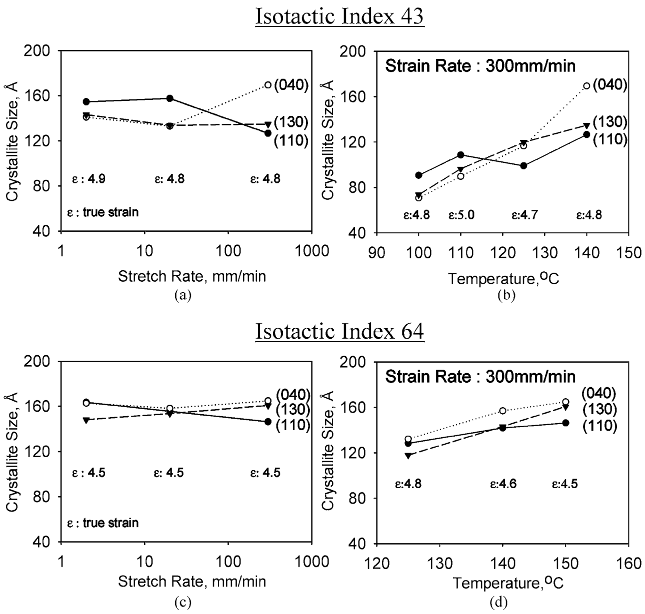

Figure 18. Crystal size obtained by WAXD dependent on stretch rate and temperature.

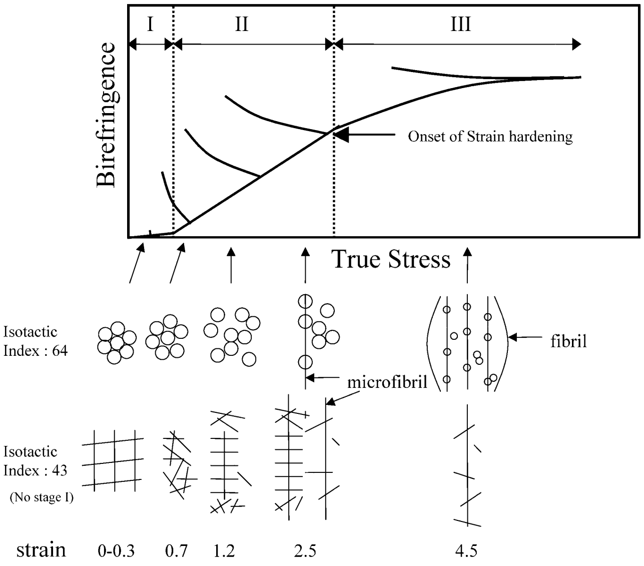

Figure 19. Schematic of the relation between property and the change of structure (isotactic index 43: 140 °C, 300 mm/min; isotactic index 64: 150 °C, 300 mm/min, strain = 3−5).

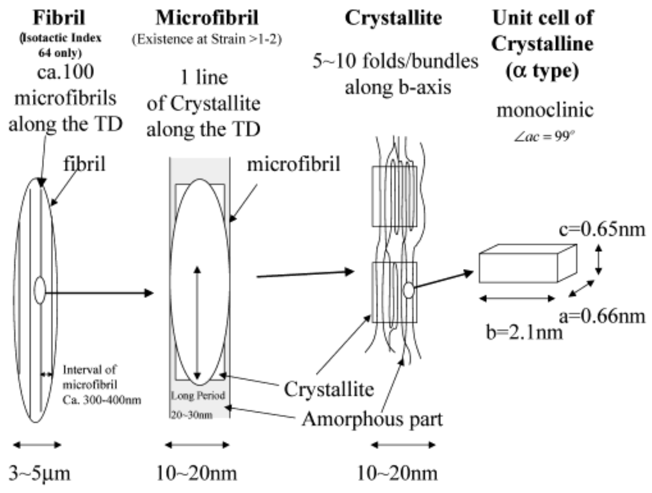

Figure 20. Schematic of the structure of stretched polypropylene (isotactic index 43: 140 °C, 300 mm/min, strain = 3−5; isotactic index 64: 150 °C, 300 mm/min, strain = 3−5).

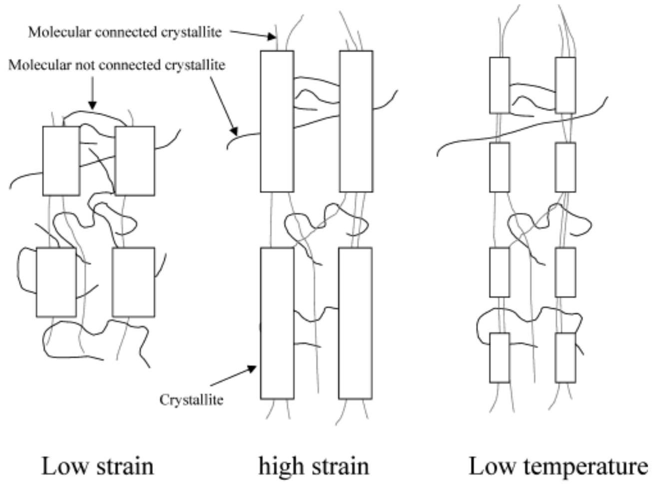

Figure 21. Schematic of the structure for explanation of the mobility of the amorphous chain in some conditions.

tures appear, and at deformation levels over strain 1.2, this morphology transforms into fibrillar superstructure with sparse population of laterally grown lamella along their lengths.

At higher isotacticity isotactic index 64, we observe macrofibrils of 3−5 μm diameter, a morphological feature that was not present at lower tacticity level. In addition, microfibrils of 10−20 nm diameter are observed in isotactic index 43 and isotactic index 64. The latter size matches well with the equatorial crystal size obtained by WAXD. A nodular superstructure that contain one or more alternating lamella−amorphous pairs was found to be promoted at lower processing temperature, lower stretching speed, and higher isotacticities, which provides plenty of room for growth of nodules, while the crystallite size obtained by WAXD indicates the width of microfibril decreases with decreasing temperature.

Stretching of low-tacticity PP was found to result in formation of crystallite/entanglement network that exerts hydrostatic pressure on the amorphous regions, leading to blooming of these regions at the surface of low-tacticity polymer.

Room temperature aging was found to coalesce these amorphous regions—a process that resembles the late stages of phase separation in partially miscible systems.

Acknowledgment. We thank the support of Asahi Kasei Corp. toward this research.

References and Notes

(1) Peterlin, A. J. *J. Polym. Sci.* **1965**, *C9*, 61−89.

(2) Ingram, P.; Kiho, H.; Peterlin, A. J. *J. Polym. Sci.* **1967**, *C16*, 1857−1868.
(3) Sakaoku, K.; Peterlin, A. J. *Makromol. Chem.* **1967**, *108*, 234−240.
(4) Hay, I. L.; Keller, A. *Kolloid Z. Z. Polym.* **1965**, *204* (1/2), 43−74.
(5) Crystal, R. G.; Hansen, D. *J. Polym. Sci.* **1968**, *A2*, 981−993.
(6) Shimamura, K. In *Morphology of Polymers. Proceedings 17th Europhysics Conference on Macromolecular Physics Pargue, Czechoslovakia, July 15−18, 1985*; Sedlacek, B., Ed.; Walter De Gruyter: Berlin, 1985; pp 319−328.
(7) Schonherr, H.; Snetivy, D.; Vancso, J. *Polym. Bull. (Berlin)* **1993**, *30*, 567−574.
(8) Snetivy, D.; Vancso, J. *Polymer* **1994**, *35*, 461−467.
(9) Magonov, S. N.; Godovsky, Y. *Am. Lab.* **1999**, *31*, 52−58.
(10) Schonherr, H.; Wiyatno, W.; Pople, J.; Frank, C. W.; Fuller, G. G.; Gast, A. P.; Waymouth, R. M. *Macromolecules* **2002**, *35*, 2654−2666.
(11) Coulon, G.; Castelein, G.; G'Sell, C. *Polymer* **1998**, *40*, 95−110.
(12) Hild, S.; Gutmannsbauer, W.; Luthi, R.; Fuhrmann, J.; Guntherodt, H. J. *J. Polym. Sci., Part B: Polym. Phys.* **1996**, *34*, 1953−1959.
(13) Rovere, A. D.; Shambaugh, R. L.; O'Rear, E. A. *J. Appl. Polym. Sci.* **2000**, *77*, 1921−1937.
(14) Hautojarvi, J.; Niemi, H. *Textile Res. J.* **2000**, *70*, 820−827.
(15) Hautojarvi, J.; Leijala, A. *J. Appl. Polym. Sci.* **1999**, *74*, 1242−1249.
(16) Risnes, O. K.; Mather, R. R.; Neville, A. *Polymer* **2003**, *44*, 89−100.
(17) Cramer, K.; Schneider, M.; Mulhaupt, R.; Cantow, H. J.; Magonov, S. N. *Polym. Bull. (Berlin)* **1994**, *32*, 637−644.
(18) Phillips, R. A.; Wolkowicz, M. D. In *Polypropylene Handbook*; Moore, E. P. J., Ed.; Hanser: Munich, 1996; Chapter 3.
(19) Brufield, D. R.; Loi, P. S. T.; Doi, Y.; Mejzik, J. *J. Appl. Polym. Sci.* **1990**, *41*, 1905−1114.
(20) Cheng, S. Z. D.; Janimak, J. J.; Zhang, A.; Hsieh, E. T. *Polymer* **1991**, *32*, 648−655.
(21) Janimak, J. J.; Cheng, S. Z. D.; Gisuti, P. A.; Hsieh, E. T. *Macromolecules* **1991**, *24*, 2253−2260.
(22) Ishikawa, M.; Sugimoto, M.; Hatada, K.; Tanaka, T. *Kobunshi Ronbunshu* **1995**, *52*, 134−40.
(23) Ishikawa, M.; Usui, K.; Kondo, Y.; Hatada, K.; Gima, S. *Polymer* **1996**, *37*, 5375−5379.
(24) Tollefson, N. M.; Johnson, C. G. *SPE ANTEC Technol. Pap.* **1999**, 2454−2457.
(25) Atul, K.; Ding, S. Y.; Ling, M. T. K.; Wood, L. *Mod. Plast.* **1999**, *76*, 95−96.
(26) Lin, S.; Waymouth, R. M. *Acc. Chem. Res.* **2002**, *35*, 765−773.
(27) Jones, T. D.; Chaffin, K. A.; Bates, F. S.; Annis, B. K.; Hagaman, E. W.; Kim, M. H.; Wignall, G. D.; Fan, W.; Waymouth, R. *Macromolecules* **2002**, *35*, 5061−5068.
(28) Wiyatno, W.; Fuller, G. G.; Pople, J. A.; Gast, A. P.; Chen, Z.; Waymouth, R. M.; Myers, C. L. *Macromolecules* **2003**, *36*, 1178−1187.
(29) Hu, Y.; Carlson, E. D.; Fuller, G. G.; Waymouth, R. M. *Macromolecules* **1999**, *32*, 3334−3340.
(30) Carlson, E. D.; Fuller, G. G.; Waymouth, R. M. *Macromolecules* **1999**, *32*, 8094−8099.
(31) Carlson, E. D.; Fuller, G. G.; Waymouth, R. M. *Macromolecules* **1999**, *32*, 8100−8106.
(32) Wiyatno, W.; Pople, J. A.; Gast, A. P.; Waymouth, R. M.; Fuller, G. G. *Macromolecules* **2002**, *35*, 8488−8497.
(33) Wiyatno, W.; Pople, J. A.; Gast, A. P.; Waymouth, R. M.; Fuller, G. G. *Macromolecules* **2002**, *35*, 8498−8508.
(34) Koike, Y.; Cakmak, M. *Polymer* **2003**, *44*, 4249−4260.
(35) Koike, Y.; Cakmak, M., to be submitted.
(36) Koike, Y.; Cakmak, M., to be submitted.
(37) Zambelli, A.; Dorman, D. E.; Richard Brewster, A. I.; Bovey, F. A. *Macromolecules* **1973**, *6*, 925−926.
(38) Zambelli. A.; Locatelli, P.; Bajo, G.; Bovey, F. A. *Macromolecules* **1975**, *8*, 687−689.
(39) Phillips, R. A.; Wolkowicz, M. D. In *Polypropylene Handbook*; Moore, E. P. J., Ed.; Hanser: Munich, 1996; pp 250 and 252.
(40) Quirk, R. P.; Alsamarraie, M. A. A In *Polymer Handbook*, 3rd ed.; Brandrup, J., Immergut, E., Eds.; Wiley: New York, 1989; pp V/23−V33.
(41) Khoury, F. *J. Res. Natl. Bur. Stand. A: Phys. Chem.* **1966**, *70A*, 29−61.
(42) Norton, D. R.; Keller, A. *Polymer* **1985**, *26*, 704−716.
(43) Phillips, P. J. *Rep. Prog. Phys.* **1990**, *53*, 549−604.
(44) Silvestri, R.; Sgarzl, P. *Polymer* **1998**, *39*, 5871−5876.

MA030250A